Digital State-feedback Control of an Interleaved DC-DC Boost Converter with Bifurcation Analysis

G. Gkizas[a,*], C. Yfoulis[b], C. Amanatidis[b], F. Stergiopoulos[b], D. Giaouris[a], C. Ziogou[c], S. Voutetakis[c], S. Papadopoulou[b,c]

[a] *School of Electrical and Electronic Engineering, Newcastle University, Newcastle Upon Tyne, United Kingdom, NE1 7RU*
[b] *Automation Engineering Department, Alexander Technological Educational Institute of Thessaloniki, 57400, Thessaloniki, P.O.Box 141, GREECE*
[c] *Chemical Process and Energy Resources Institute (C.P.E.R.I.) Centre for Research and Technology Hellas (CE.R.T.H.), 6th km Harilaou-Thermis, GR-57001, Thermi, Thessaloniki, GREECE*

Abstract

This paper evaluates several state-feedback control design methods for a multi-phase interleaved DC-DC boost converter with an arbitrary number of legs. The advantages of state-feedback control laws are numerus since they do not burden the system with the introduction of further zeros or poles that may lead to poorer performance as far as overshoot and disturbance rejection is concerned. Both static and dynamic full state-feedback control laws are designed based on the converter's averaged model. Building on previous work, this paper introduces significant extensions on the investigation of several undesirable bifurcation phenomena. In the case of static state-feedback it is shown that interleaving can give rise to more severe bifurcation phenomena, as the number of phases is increased, leading to multiple equilibria. As a remedy, a bifurcation analysis procedure is proposed that can predict the generation of multiple equilibria. The novelty of this paper is that this analysis can be integrated into the control design so that multiple equilibria can be completely avoided or ruled out of the operating region of interest. The proposed control laws are digitally implemented and validated in a 2-leg case study using both simulation and experimentation.

[*] Corresponding author. Fax: +44 (0) 191 208 8180. This paper was not presented at any IFAC meeting.
Email addresses: g.gkizas2@ncl.ac.uk (G. Gkizas), cyfoulis@autom.teithe.gr (C. Yfoulis), amanatidis.xrhstos@gmail.com (C. Amanatidis), fstergio@autom.teithe.gr (F. Stergiopoulos), damian.giaouris@newcastle.ac.uk (D. Giaouris), cziogou@cperi.certh.gr (C. Ziogou), paris@cperi.certh.gr (S. Voutetakis), shmira@autom.teithe.gr (S. Papadopoulou)

Keywords: Interleaved boost DC-DC converters, static state-feedback, dynamic state-feedback, multiple equilibria

1. Introduction

Nowadays, DC-DC power converters play a vital role in a wide range of applications, from their utilization in common electronic devices such as laptops and mobile phones to larger scale industrial applications such as modern electric vehicles and power systems. One common feature encountered among these switched-mode power converters is the output current and voltage ripple that can be accounted to their switching action. In the design process of the switched-mode power converters the requirements for small current and voltage ripples, within desired limits, as well as high efficiency must be met. Interleaving not only can alleviate the situation since it reduces ripples and improves efficiency but it also allows for the size reduction of inductors and capacitors. As the requirements for efficient power converters become more and more demanding the interleaving structure constitutes a powerful tool for meeting these design objectives.

The development of highly efficient power converter systems is quite important in modern power grid applications. A feasible path to achieve high efficiency in wide-range operating conditions is the systematic design of robust and efficient control laws which address the inherent nonlinear dynamics while respecting additional constraints. This is the main reason for which the problem of designing advanced control algorithms for switched mode DC-DC converters has attracted considerable interest in recent years. Such converters possess special characteristics and are particularly challenging from a control point of view for a number of reasons. For example, they usually operate in the presence of unpredictable disturbances (supply voltage and load variations) while a reliable fast and accurate static and dynamic performance in a wide operating range, and under hard state and control constraints, is also required.

The nature of their dynamics is quite complex since they are highly nonlinear [1, 2, 3] and hybrid in nature due to involvement of high-frequency switching. These facts pose many challenges when it comes to their control design. The predominant

method for eliminating the switching action of the converter in order to derive a suitable model that can be used for directly applying control theory is averaging. The resulting average model is a good approximation that can be used as the basis for control design since the nonlinear traits of the converter, such as bilinear terms, and state and control saturations are retained. However, when it comes to the actual implementation of the control laws, either in analog or digital form, the neglected switched dynamics are still in force due to the employment of Pulse-Width Modulation (PWM). The switched dynamics burden the system with other kinds of instabilities, called limit cycle instabilities or bifurcations, that the average model cannot predict or deal with, for a recent review see e.g. [4]. The impact of these kind of instabilities on the converter can severely affect the efficiency and its lifetime since they can double the harmonic content (fast-scale bifurcation) or in other cases superimpose a low frequency and high amplitude harmonic(slow-scale bifurcation). However, when it comes to saddle-node bifurcations the averaged model can be informative since its nonlinear nature can provide knowledge on their existence.

It is common practice for conventional control techniques to be used along with linearized models so that linear feedback laws are derived, which have the advantage of simplicity and low-cost implementation. However, these approaches may lead to deteriorated performance or even unpredictable behaviour, due to the uncertainties and the nonlinearities of the converter. Although popular industrial standard control schemes, i.e. PI, voltage-mode and current-mode control are used successfully even in nonlinear converters, their linear and time-invariant form does not guarantee robust stability and performance in non-nominal operating conditions.

To this end, many advanced robust linear and nonlinear state-feedback control techniques for bilinear boost DC-DC converters have been proposed recently in the literature. These include Model Predictive Control (MPC) [5, 6, 7], constrained stabilization [8], Linear Matrix Inequalities (LMI) convex optimization control synthesis methods [9, 10, 11, 12, 13], and passivity-based control [14]. Moreover, other advanced control techniques have been suggested for the boost converter, including sliding-mode control [15, 16, 17], and robust control design [18, 19] . Although some of these techniques have been tested to parallel/interleaved buck or boost DC-DC converters

[20, 21, 22, 23] and several studies for their mathematical modeling and control have recently appeared [24, 25, 26, 27, 28] the lack of constraints concerning the nonlinear phenomena that are presents due to the bilinear dynamics is noticeable.

For a simple boost converter case study, systematic constrained stabilization techniques have been also derived by the authors for designing robust state feedback laws such that further state and control constraints are satisfied [29, 30, 31]. These techniques provide guarantees not only for nominal operating conditions, but also in a wide operating range defined by a-priori specified parameter variation intervals. They have been developed for static state feedback control laws, in the ideal (lossless) case, in which non idealities due to the inductor's series resistance are assumed to be negligible. In this paper these ideas and tools of the constrained stabilization are fully extended from a simple boost to the multi-phase interleaved boost converter, including nonidealities occurring from inductor's series resistance. Some initial research results of this work concerning the study of multiple equilibria generation have recently appeared in [32]. The present paper provides significant extensions of the main ideas in [32] supported by detailed mathematical analysis.

A further important contribution of this work is the consideration of *dynamic* state-feedback control laws that relieves the system from the existence of multiple equilibria, due to the effect of the integrator state introduced in the system. The addition of the integrating action in the system allows for the design of control laws that are relieved from constraints concerning multiple equilibria that may introduce conservatism. Pole placement techniques are utilized to design appropriate control laws that will compensate the system both in the static and dynamic state-feedback case.

This paper is organized as follows. In section 2 we begin with an introduction to the interleaved converter topology followed by its mathematical modeling in two different forms, exact switched and averaged. In section 3 a novel bifurcation analysis procedure is introduced, which allows the prediction and avoidance of multiple equilibria, based on the converter's bilinear averaged model. Section 4 presents our main control design techniques in a static or dynamic state-feedback control law form using the linearized averaged model and complementary bifurcation criteria. The control law's digital implementation is next discussed in section 5. Section 6 concludes the paper

with a successful proof of concept for a specific interleaved boost case study, using both simulation and experimental results.

Notation : In this paper, $\mathbb{R}$ denotes the real numbers and $\mathbb{R}^n$ is the vector space of n-dimensional real vectors. Boldface upper case letters denote matrices, while boldface lower case letters are used for vectors. All vectors are assumed to be column vectors.

2. Mathematical modeling

An interleaved boost converter is the result of connecting several simple boost converters in parallel. An N-legged converter topology is shown in Figure 1. As it can be seen from Figure 1 each phase is comprised of an inductor, a diode and a switch. For properly implementing the interleaving principle every pulse width modulator must be introduced with a phase difference of $2\pi/N$ relative to each leg, with N being the number of legs.

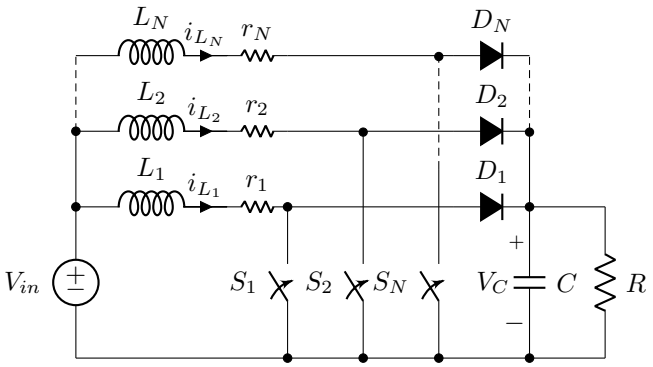

Figure 1: Interleaved DC-DC Boost converter with N-legs.

Since the system is subject to switching, i.e. changes in the topology that depend on the states of the switches, the analytical description of the dynamics of the converter corresponds to a piecewise linear system of differential equations, called the *exact switched model*. In the general case of an N-leg topology, the state vector may be defined as

$$\mathbf{x}(t) = [\, x_1(t)\, x_2(t)\, \ldots\, x_{N+1}(t)\,]^T \tag{1}$$

where $x_1(t)$ is the capacitor voltage V_C and $x_{j+1}(t)$, $j = 1, 2, 3, \ldots, N$ are the j-th leg inductor currents i_{L_j}. Assuming that the converter operates in CCM (continuous conduction mode), the inductor current x_{j+1} [1] of the j-th phase is governed by

$$\dot{x}_{j+1} = \frac{1}{L_j} \cdot \left(V_{in} - s'_j \cdot x_1 - r_j \cdot x_{j+1}\right) \quad j = 1, 2, \ldots, N \tag{2}$$

where $s'_j = 1 - s_j$, and s_j is the switching function of the j-th active switch. $s_j = 1$ implies that the corresponding active switch S_j is turned on, while if $s_j = 0$, S_j is turned off. The capacitor voltage equation is given by

$$\dot{x}_1 = \frac{1}{C} \cdot \left(\sum_{j=1}^{N} s'_j \cdot x_{j+1} - \frac{1}{R} \cdot x_1 \right) \tag{3}$$

where L_j, r_j is the j-th leg inductance and series resistance, C is the output capacitance and R is the load resistance. V_{in} is the input (supply) voltage. If not otherwise stated, throughout the paper a symmetrical topology is assumed, hence the inductors have the same inductance and series resistance, i.e. $r_j = r$, $L_j = L$.

For the sake of simplicity a 2-legged topology will be considered throughout this paper as far as the control laws application and experimental verification are concerned. Nevertheless, the underlying analysis will be conducted considering an arbitrary number of legs. According to the previous analysis, the exact switched dynamics of a 2-leg interleaved converter are

$$\dot{\mathbf{x}} = \begin{cases} \mathbf{A}_{s1}\,\mathbf{x} + \mathbf{b}\,V_{in} & S_1 = ON \quad S_2 = OFF \\ \mathbf{A}_{s2}\,\mathbf{x} + \mathbf{b}\,V_{in} & S_1 = OFF \quad S_2 = ON \\ \mathbf{A}_{on}\,\mathbf{x} + \mathbf{b}\,V_{in} & S_1 = ON \quad S_2 = ON \\ \mathbf{A}_{off}\,\mathbf{x} + \mathbf{b}\,V_{in} & S_1 = OFF \quad S_2 = OFF \end{cases} \tag{4}$$

$$\mathbf{A}_{s1} = \begin{bmatrix} \frac{-1}{RC} & 0 & \frac{1}{C} \\ 0 & \frac{-r}{L} & 0 \\ \frac{-1}{L} & 0 & \frac{-r}{L} \end{bmatrix}, \; \mathbf{A}_{s2} = \begin{bmatrix} \frac{-1}{RC} & \frac{1}{C} & 0 \\ \frac{-1}{L} & \frac{-r}{L} & 0 \\ 0 & 0 & \frac{-r}{L} \end{bmatrix} \tag{5}$$

[1] The independent variable of time, t, will be omitted from this point on unless otherwise noted.

$$\mathbf{A}_{on} = \begin{bmatrix} \frac{-1}{RC} & 0 & 0 \\ 0 & \frac{-r}{L} & 0 \\ 0 & 0 & \frac{-r}{L} \end{bmatrix}, \mathbf{A}_{off} = \begin{bmatrix} \frac{-1}{RC} & \frac{1}{C} & \frac{1}{C} \\ \frac{-1}{L} & \frac{-r}{L} & 0 \\ \frac{-1}{L} & 0 & \frac{-r}{L} \end{bmatrix} \tag{6}$$

$$\mathbf{b} = [0\ 1/L\ 1/L]^T \tag{7}$$

However, the switched dynamics of the system does not allow for control theory to be applied directly thus the procedure of averaging must take place to eliminate the switching action. The *average* model is an approximation of the the *exact switched model* but certainly more amenable to control design. This model can be described by the same equations (2), (3) if all state variables are replaced by their averaged versions and the switching functions s_j are replaced by the duty cycle functions d_j, which are our control inputs, i.e. $u_j = d_j$. Thus, the following equations are derived

$$\begin{aligned} \dot{x}_1 &= \frac{1}{C} \cdot \left(\sum_{j=1}^{N} x_{j+1} \cdot u'_j - \frac{1}{R} \cdot x_1 \right) \\ \dot{x}_{j+1} &= \frac{1}{L} \cdot \left(V_{in} - x_1 \cdot u'_j - r \cdot x_{j+1} \right) \end{aligned} \tag{8}$$

In a 2-leg topology, the procedure of averaging renders the control inputs u_1, u_2 equivalent to the duty cycles d_1, d_2 of the switches s_1, s_2, respectively. Hence, after some manipulations the nonlinear (bilinear) averaged dynamics of a 2-leg converter can be expressed as

$$\dot{\mathbf{x}} = \mathbf{A}_1 \cdot \mathbf{x} + \mathbf{A}_2 \cdot \mathbf{x} \cdot u_1 + \mathbf{A}_3 \cdot \mathbf{x} \cdot u_2 + \mathbf{b} \cdot V_{in} \tag{9}$$

where $\mathbf{A}_1 = \mathbf{A}_{off}$ and $\mathbf{A}_2 = \mathbf{A}_{s1} - \mathbf{A}_{off}$, $\mathbf{A}_3 = \mathbf{A}_{s2} - \mathbf{A}_{off}$.

In a general N-leg topology the corresponding bilinear dynamics take the general form

$$\dot{\mathbf{x}} = \mathbf{A}_1 \cdot \mathbf{x} + \sum_{k=1}^{N} \mathbf{A}_{k+1} \cdot \mathbf{x} \cdot u_k + \mathbf{b} \cdot V_{in} \tag{10}$$

where the corresponding matrices $\mathbf{A}_{k+1}$ can be similarly defined as $\mathbf{A}_{k+1} = \mathbf{A}_{sk} - \mathbf{A}_{off}$.

2.1. Open-loop steady-state analysis

Since the inductor parasitic resistances are not considered negligible an open-loop steady-state analysis can be very informative as far as their impact on the operation of the converter is concerned. It should be noted that in this case these resistances are modeled to incorporate other losses as well, that may stem from the rest of the components of the system. The values of the parasitic resistances are experimentally validated in section 6 and utilized in the control design procedure.

The simplest, but also quite common case in practice is a *balanced* situation , in which the total current is equally shared among all legs and the parasitic series inductor resistances are considered symmetric, i.e. each having the same resistance value. In this case, the same steady-state currents I_{ss} [2] and duty cycles u_{ss} for the control inputs u_j applied to each leg are encountered. By equating derivatives of (8) to zero, we deduce that all possible equilibria satisfy

$$0 \quad = \quad -x_1 \, + \, R \cdot \left(\sum_{j=1}^{N} x_{j+1} \, u'_j \right) \tag{11}$$

$$0 \quad = \quad V_{in} - x_1 \, u'_j - r \, x_{j+1} \tag{12}$$

Simple algebraic manipulations lead to (13), where u'_{ss} is replaced by $1 - u_{ss}$ and N is the number of legs.

$$V_{ss} = \frac{N \, R \, V_{in} (1 - u_{ss})}{r \, + \, N \, R (1 - u_{ss})^2} \; , \; I_{ss} = \frac{V_{in}}{r \, + \, N \, R (1 - u_{ss})^2} \tag{13}$$

Equations in (13) can be further utilized in order to investigate the impact of the inductor series resistance on the operation of the system. For example, differentiating w.r.t. to the steady-state duty cycle u_{ss} and equating the derivative to zero the maximum operating point $(u_{ss}^{max}, V_{ss}^{max})$ is found to be

$$u_{ss}^{max} = 1 - \sqrt{\frac{r}{N \, R}} \; , \; V_{ss}^{max} = \sqrt{\frac{N \, R}{r}} \, \frac{V_{in}}{2} \tag{14}$$

What can be deduced from (14) is that as the series resistance becomes smaller and the number of legs increases the maximum operating point moves to higher values.

[2] Subscript ss denotes the steady state value, i.e. when $\dot{\mathbf{x}} = 0$, of the system's dependent variables.

Moreover, there are always two solutions for u_{ss} which are

$$u_{ss} = 1 - \frac{V_{in} \pm \sqrt{V_{in}^2 - \frac{4\,r\,V_{ss}^2}{N\,R}}}{2\,V_{ss}} \tag{15}$$

The solution of interest in the domain $u_{ss} \in [\,0\,,\,u_{ss}^{max}\,]$ is

$$u_{ss} = 1 - \frac{V_{in} + \sqrt{V_{in}^2 - \frac{4\,r\,V_{ss}^2}{N\,R}}}{2\,V_{ss}} \tag{16}$$

from which (13) also yields

$$I_{ss} = \frac{V_{in} - \sqrt{V_{in}^2 - \frac{4\,r\,V_{ss}^2}{N\,R}}}{2\,r} \tag{17}$$

A graphical interpretation of this argument can be seen in Figure 6 for the experimental setup of section 6. The domain of interest, as far as the V_{ss} is concerned, is between the input voltage V_{in} and the maximum operating Voltage V_{ss}^{max} (point Q in Figure 6). However, for a V_{ss} value laying inside this domain there is also another solution for u_{ss} and I_{ss}, given in equation (13), on the right of the maximum operating point (e.g. for $V_{ss} = 10V$ the two solutions are obtained at the points P_1, P_2 shown explicitly in Figure 6). The operation of the converter near the maximum point Q should be avoided due to the increased power loss.

3. Bifurcation analysis of bilinear dynamics under static state feedback

Recently, the problem of multiple equilibria (saddle-node or Hopf bifurcation) generation for a boost converter under static state feedback has been fully investigated in [31]. In this section this analysis is extended to an interleaved boost converter.

The bifurcation analysis that follows investigates the existence of multiple equilibria in the case where the duty cycle functions are specified by a state-feedback control law, i.e. it is a *closed-loop* steady-state analysis. Hence, the *open-loop* steady-state analysis of the previous section does not suffice, and the control law expression must be taken into account.

Multiple equilibria are attributed to the nonlinear (bilinear) dynamics of the converter, hence we proceed with a steady-state mathematical analysis on the basis of (8), combined with the control law's mathematical expression.

A general static state-feedback control law for the duty cycle functions is given by

$$u_j \;=\; k_1 \cdot [x_1 \;-\; V_{ss}] \;+\; k_2 \cdot [x_{j+1} \;-\; I_{ss}] \;+\; u_{ss} \tag{18}$$

where it is assumed that the feedback gains k_1, k_2 are the same for all legs. By separating dynamic and static elements we may express $u'_j(t) = 1 - u_j(t)$ with the help of (18) as

$$u'_j \;=\; -k_1 \cdot x_1 \;-k_2 \cdot x_{j+1} \;+\; \varepsilon \tag{19}$$

where

$$\varepsilon \;=\; 1 - u_{ss} + k_1\, V_{ss} + k_2\, I_{ss} \tag{20}$$

The next step is to solve (12) for x_{j+1} and replace back to (11) to yield a polynomial in x_1 only. Assume for the moment that a series resistance mismatch occurs, i.e. different resistance values r_j for each leg are encountered. Combining (12) and (19) yields

$$x_{j+1} \;=\; \frac{V_{in} \;+\; k_1 \cdot x_1^2 \;- \varepsilon \cdot x_1}{r_j - k_2 \cdot x_1} \tag{21}$$

Similarly, combining (11) and (19) results in

$$R \cdot \left(\sum_{j=1}^{N} \left[(\varepsilon - k_1 x_1) \cdot x_{j+1} - k_2 \cdot x_{j+1}^2 \right] \right) \;=\; x_1 \tag{22}$$

Now the expressions from (21) may be used in (22) to yield a polynomial in x_1 only. Due to the quadratic terms x_{j+1}^2 the expressions $(r_j - k_2 \cdot x_1)^2$ will appear in the denominator, hence if both sides are multiplied by these terms the following equation in x_1 is obtained

$$\begin{aligned} & R \cdot \sum_{j=1}^{N} \left\{ \prod_{i=1, i\neq j}^{N} (r_i - k_2\, x_1)^2 \, \left[\Theta\, (r_j - k_2\, x_1) \;-\; k_2\, \Xi \right] \right\} \\ & =\; x_1 \cdot \prod_{j=1}^{N} (r_j - k_2\, x_1)^2 \end{aligned} \tag{23}$$

where the quantities Θ, Ξ are given by

$$\begin{aligned} \Theta \;&=\; (\varepsilon - k_1 \cdot x_1) \cdot (V_{in} \;+\; k_1 \cdot x_1^2 \;- \varepsilon \cdot x_1) \\ \Xi \;&=\; \left(V_{in} \;+\; k_1 \cdot x_1^2 \;- \varepsilon \cdot x_1\right)^2 \end{aligned} \tag{24}$$

These complex expressions can be useful for a computer numerical solution. However, this formulation allows us to observe that in the general case the order of the resulting equation is $(2 \cdot N + 1)$, i.e. linearly increasing with the number of phases $N \geq 2$.

In the absence of any series resistance mismatch, in which $r_j = r$, (23) becomes

$$R \cdot N \cdot \left[\Theta\left(r - k_2\, x_1\right) \,-\, k_2\, \Xi\right] \,=\, x_1 \cdot \left(r - k_2\, x_1\right)^2 \tag{25}$$

resulting in a 4th order equation regardless of the number of phases. However, from (24),(25) it can be easily seen that the coefficient of the fourth power of x_1 will always be zero, since the corresponding terms in the expression $\left[\Theta\left(r - k_2 x_1\right) \,-\, k_2\, \Xi\right]$ are canceled out. Hence, it is possible after some algebraic manipulations to arrive at an analytical expression of the resulting equation as

$$\alpha_3\, x_1^3 \,+\, \alpha_2\, x_1^2 \,+\, \alpha_1\, x_1 \,+\, \alpha_0 \,=\, 0 \tag{26}$$

which is a cubic in x_1, where the coefficients $\alpha_i\,,\; i \,=\, 0, \ldots, 3$ are functions of all parameters involved and are given by

$$\begin{aligned}
\alpha_3 &= -k_2^2 \,-\, N\, R\, r\, k_1^2 \\
\alpha_2 &= 2\, r\, k_2 \,+\, N\, R\, \left(2\, \varepsilon\, r\, k_1 - k_1\, k_2\, V_{in}\right) \\
\alpha_1 &= -r^2 \,-\, N\, R\left(r\, \varepsilon^2 \,+\, r\, k_1\, V_{in} \,-\, \varepsilon\, V_{in}\, k_2\right) \\
\alpha_0 &= N\, R\, V_{in}\left(r\, \varepsilon \,-\, k_2\, V_{in}\right)
\end{aligned} \tag{27}$$

The variable $\varepsilon = 1 - u_{ss} + k_1\, V_{ss} + k_2\, I_{ss}$ contains all setpoint values V_{ss}, I_{ss}, u_{ss}, which can be further eliminated with the help of (13),(16). Then we have

$$\varepsilon = k_1 \cdot V_{ss} + \frac{V_{in} + \sqrt{E}}{2V_{ss}} + k_2 \cdot \frac{V_{in} - \sqrt{E}}{2r}\,,\; E = V_{in}^2 - \frac{4rV_{ss}^2}{NR} \tag{28}$$

All formulas derived in this section provide significance assistance for finding all possible equilibria and specifying bifurcation curves by solving simple algebraic equations numerically.

However, it is clear that even in the absence of any series resistance mismatch, in the *non-ideal* case where $r \,\neq\, 0$ the resulting expressions are too complex to allow a further analytical investigation. Nevertheless, in order to gain useful insight into the interleaving process, w.r.t. to the multiple equilibria generation problem, we will consider the *ideal* case and extend the corresponding analysis of [31] in the following section.

3.1. Bifurcation analysis in the ideal case

In this case the series resistance vanishes and the expression (26) can be easily brought in a cubic form $f(x_1) = 0$ with real coefficients that may give one to three real equilibria, where

$$f(x_1) = x_1^3 + z \cdot x_1^2 + p \cdot x_1 + q \tag{29}$$

From (27) it can be deduced that

$$\begin{aligned} z &= \frac{V_{in} k_1 R}{k_2} \cdot N \, , \, p = -V_{ss}^2 - N \cdot R \cdot \frac{V_{in}(k_1 V_{ss}^2 + V_{in})}{V_{ss}\, k_2} \\ q &= N \cdot R \cdot \frac{V_{in}^2}{k_2} \end{aligned} \tag{30}$$

In this case we also have much simpler expressions for I_{ss}, u_{ss}, i.e.

$$I_{ss} = \frac{1}{N} \cdot \frac{V_{in}}{R(1-u_{ss})^2} = \frac{1}{N} \cdot \frac{V_{ss}^2}{R V_{in}} \, , \, u_{ss} = 1 - \frac{V_{in}}{V_{ss}} \tag{31}$$

These expressions allow an analytical investigation similar to the one followed in [31] for a simple boost converter. Although all results in [31] can be extended to the interleaved case, in the sequel we present extensions of Proposition 1 and Lemmas 3,4, with proofs very similar to [31]. These results are enough to give us a good flavour and useful insights of the effect of interleaving to bifurcations. Once again we consider equilibria voltages $V_{ss} > V_{in}$ and feedback gains satisfying $k_1 > 0, k_2 < 0$ and the following definition :

Definition 1 *A bilinear system (11),(12) in the balanced and ideal case with one, two or three real equilibria is denoted as EQ 1, EQ 2 and EQ 3, respectively.*

In the interleaving case we have a new *bifurcation function*, with an extra variable, i.e. the number of legs N

$$\begin{aligned} \Gamma(V_{ss}, V_{in}, R, k_1, k_2, N) = V_{ss}^3 \, k_2^2 + V_{ss} V_{in}^2 R^2 k_1^2 \cdot N^2 \\ + 4 R V_{in}^2 k_2 \cdot N + 2 V_{in} R V_{ss}^2 k_1 k_2 \cdot N \end{aligned} \tag{32}$$

and the following updated proposition

Proposition 1 *The bilinear system (11),(12) in the balanced and ideal case controlled by a state-feedback law (18) exhibits one to three real equilibria and it is*

1. *EQ 1 if and only if* $\Gamma < 0$
2. *EQ 2 if and only if* $\Gamma = 0$
3. *EQ 3 if and only if* $\Gamma > 0$

The following lemmas related to the multiple equilibria avoidance are of particular interest.

Lemma 1 *A sufficient condition for the absence of positive multiple real equilibria of (29) is the satisfaction of the following inequality*

$$\left|\frac{k_1}{k_2}\right| < \frac{1}{N} \cdot \frac{V_{ss}}{R \cdot V_{in}} \tag{33}$$

However, imposing conditions to ensure the absence of any bifurcation phenomena whatsoever can be very restrictive. Less conservative conditions which ensure the absence of any multiple equilibria inside a specific region of interest may be found. E.g. simple state constraints for the output voltage $0 \leq V_C \leq V_C^+$ may be included. The following lemma covers this case.

Lemma 2 *A necessary and sufficient condition for the absence of positive multiple real equilibria of (29) in the interval $V_C \leq V_C^+$, is the satisfaction of the following inequality*

$$N \cdot (RV_{in}V_{ss}V_C^+)\, k_1 + (V_{ss} + V_C^+)V_{ss}V_C^+ k_2 - N \cdot RV_{in}^2 < 0 \tag{34}$$

Figure 2 provides a pictorial presentation of the previous results that allows the extraction of useful information and insights. As proved in [31] the bifurcation curve $\Gamma = 0$ is a parabola, made of two separate non-intersecting curves in the quadrant of interest (the first quadrant of the $V_{in} - R$ plane, or the fourth quadrant of the $k_1 - k_2$ plane). This property can be shown to hold for the interleaving case as well. For comparison purposes we have used the same numerical data as in [31] and considered a variable number of legs $N = 1, 2, 3$ to study the effect of interleaving. The result is presented in Figure 2(a),(b). Either $V_{in} - R$ or $k_1 - k_2$ bifurcation diagrams show clearly that as the number of phases increases the curves are moved to lower values, hence the bifurcation phenomena occurrence is much more frequent, i.e. for smaller

deviations from the nominal values (as seen on the $V_{in} - R$ plane) or for a wider variety of feedback gains (on the $k_1 - k_2$ plane).

The effect on the $k_1 - k_2$ plane is particularly important since this diagram has been directly used in [31] for controller design, i.e. for the selection of appropriate gains, such that any multiple equilibria generation is completely avoided, or at least sufficiently suppressed (as suggested by Lemmas 1,2). To judge this, we present a detailed and clearer picture in Figure 2(c). For the area of interest ($0 \leq k_1 \leq 0.1$, $-1 \leq k_2 \leq 0$)[3] the same bifurcation curves $\Gamma = 0$ as in Figure 2(b) are shown (the upper part only), together with the bifurcation lines produced by the results of Lemmas 1,2. Again, it is obvious that the slope of these lines increases with N, leaving less and less space for appropriate gain selection. This can be also analytically confirmed by considering the corresponding mathematical expressions. The line equation implied by (33) can be reformulated as

$$k_2 \; = \; -N \cdot m \cdot k_1 \;\; , \;\; m = \frac{R \cdot V_{in}}{V_{ss}} \tag{35}$$

i.e. is forms a line with negative slope equal to $N \cdot m$ and zero intercept. Similarly, the line expression implied by (34) can be rewritten as

$$k_2 \; = \; -N \cdot m \cdot k_1 \; + \; N \cdot b \tag{36}$$

i.e. it is clearly a line with negative slope equal to $N \cdot m$ and intercept equal to $N \cdot b$, where

$$m = \frac{R \cdot V_{in}}{V_C^+ + V_{ss}} \;\; , \;\; b = \frac{R \cdot V_{in}^2}{V_{ss} V_C^+ (V_{ss} + V_C^+)} \tag{37}$$

Another observation from Figure 2(c) is that, compared with the exact bifurcation boundary $\Gamma = 0$, the bifurcation lines produced by (35) according to Lemma 1 (shown at the left bottom part) are certainly quite conservative, while the bifurcation lines produced by (37) according to Lemma 2 (depicted next to the curves where $\Gamma = 0$) offer an improved result, i.e. a larger admissible area for gain selection.

Finally, although all previous results have been presented for the ideal case, which allows analytical verification, they are representative of the more general non-ideal

[3] This choice for the area of interest, i.e. $k_1 > 0$ and $k_2 < 0$, provides a stable system with high damping [33].

case, in which $r \neq 0$. Similar analysis can be carried out using the corresponding cubic of (27) in order to specify a new bifurcation function Γ. This has be done numerically in MATLAB and representative cases are depicted in Figure 3. The effect of increasing the number of legs N is the same as in the ideal case, i.e. it allows less freedom in the gain selection-control design process. The series resistance value does not have a significant effect in the result, since the bifurcation curve is moved slightly upwards when its value is increased.

4. State-feedback control design

In this work, both static and dynamic full state-feedback control laws have been studied for controlling an N-leg interleaved converter. The design methods are based on the linearized dynamics of the bilinear interleaved converter and pole placement techniques are considered. However, their novelty lies in the use of complementary bifurcation analysis. In a balanced situation, the design can be performed using two dimensional dynamics, due to symmetry. This is a common practice followed in other works as well [25, 27].

4.1. Static state-feedback design using the linearized averaged model and bifurcation analysis

The static state-feedback control law is given by (18), i.e.

$$u_j = k_1 \cdot [x_1 - V_{ss}] + k_2 \cdot [x_{j+1} - I_{ss}] + u_{ss} \tag{38}$$

where u_j is the control input (duty cycle) applied to the j-leg, $j = 1, 2, \ldots, N$. At this point it should be noted that, although the feedback gains are the same for all legs, all inductor currents are independently measured and utilized by the control law (38) for each corresponding leg. Fortunately, the system of differential equations (8) that govern the interleaved converter that is comprised by an arbitrary number of legs can be significantly simplified due to symmetry. Thus instead of having a $(N+1) \times (N+1)$ system of equations that describes an N legged converter it can be conveniently

truncated using (8) to the following 2×2 system

$$\begin{aligned} \dot{x}_1 &= \frac{1}{C} \cdot \left(N \cdot x_2 \cdot u' - \frac{1}{R} \cdot x_1 \right) \\ \dot{x}_2 &= \frac{1}{L} \cdot (V_{in} - x_1 \cdot u' - r \cdot x_2) \end{aligned} \tag{39}$$

where x_2 is a state variable representing any of the equally balanced leg's inductor current, $u' = 1 - u$, and u is the input (duty cycle) expressed in closed-loop form as

$$u = k_1 \cdot [x_1(t) - V_{ss}] + k_2 \cdot [x_2(t) - I_{ss}] + u_{ss} \tag{40}$$

This truncated system can be expressed in matrix-vector form similarly to (10) as follows

$$\dot{\mathbf{x}} = \mathbf{A}_1 \cdot \mathbf{x} + \mathbf{A}_2 \cdot \mathbf{x} \cdot u + \mathbf{b} \cdot V_{in} \tag{41}$$

where

$$\mathbf{A}_1 = \begin{bmatrix} \frac{-1}{RC} & \frac{N}{C} \\ \frac{-1}{L} & \frac{-r}{L} \end{bmatrix}, \mathbf{A}_2 = \begin{bmatrix} 0 & \frac{-N}{C} \\ \frac{1}{L} & 0 \end{bmatrix}, \mathbf{b} = \begin{bmatrix} 0 \\ 1/L \end{bmatrix} \tag{42}$$

The next step is to apply a linear transformation so that the non-zero equilibrium is mapped to the zero state. The new state variables are the error variables $\mathbf{x}_e$ and input u_e such that

$$\mathbf{x}_e = \mathbf{x} - \mathbf{x}_{ss} \text{ and } u_e = u - u_{ss} \tag{43}$$

so that (41) yields a new auxiliary bilinear system

$$\begin{aligned} \dot{\mathbf{x}}_e &= \mathbf{A} \cdot \mathbf{x}_e + \mathbf{A}_2 \cdot \mathbf{x}_e \cdot u_e + \mathbf{b}_2 \cdot u_e \\ \mathbf{A} &= \mathbf{A}_1 + \mathbf{A}_2 \cdot u_{ss}\,, \mathbf{b}_2 = \mathbf{A}_2 \cdot \mathbf{x}_{ss} \end{aligned} \tag{44}$$

The linearized dynamics are given by

$$\begin{aligned} \dot{\mathbf{x}}_e &= \mathbf{A} \cdot \mathbf{x}_e + \mathbf{b}_2 \cdot u_e \\ \mathbf{A} &= \begin{bmatrix} -\frac{1}{RC} & N \cdot \frac{u'_{ss}}{C} \\ -\frac{u'_{ss}}{L} & -\frac{r}{L} \end{bmatrix}, \mathbf{b}_2 = \begin{bmatrix} -N \cdot \frac{I_{ss}}{C} \\ \frac{V_{ss}}{L} \end{bmatrix} \end{aligned} \tag{45}$$

As in (38), we consider control laws in an affine state-feedback form, which for a non-zero equilibrium $\mathbf{x}_{ss}$ and corresponding input u_{ss} are stated as

$$u = \mathbf{k}^T \cdot (\mathbf{x} - \mathbf{x}_{ss}) + u_{ss} \text{ or } u_e = \mathbf{k}^T \cdot \mathbf{x}_e \tag{46}$$

for a state vector $\mathbf{k} = [k_1\, k_2]^T$. Combining (45),(46) we arrive at a linear closed-loop system with a system matrix

$$\mathbf{A}_{lin} = \begin{bmatrix} -\frac{1}{RC} - N\,\frac{I_{ss}}{C}\,k_1 & N\,\frac{1}{C}(u'_{ss} - I_{ss}\,k_2) \\ \frac{1}{L}(V_{ss}\,k_1 - u'_{ss}) & \frac{1}{L}(V_{ss}\,k_2 - r) \end{bmatrix} \tag{47}$$

Further manipulations suggest that the characteristic polynomial of (47) is $p = |sI_2 - \mathbf{A}_{lin}| = s^2 + a_1 s + a_0$, where

$$\begin{aligned} a_1 &= N\,\tfrac{I_{ss}}{C}\,k_1 - \tfrac{V_{ss}}{L}\,k_2 + \tfrac{r}{L} + \tfrac{1}{RC} \\ a_0 &= N\,\tfrac{1}{LC}(rI_{ss} - u'_{ss}V_{ss})\,k_1 - N\,\tfrac{1}{LC}(V_{ss} + u'_{ss}I_{ss})\,k_2 \\ &\quad + \tfrac{r}{RLC} + N\,\tfrac{u'^2_{ss}}{LC} \end{aligned} \tag{48}$$

It is evident that the necessary and sufficient condition for the system to be stable, i.e. that the eigenvalues have negative real part, is that $a_1 > 0$ and $a_0 > 0$. Moreover, a second order characteristic equation $s^2 + 2\zeta\omega_n s + \omega_n^2$ implies that $a_1 = 2\zeta\omega_n$ and $a_0 = \omega_n^2$. These considerations allow the extraction of simple and convenient expressions concerning stability and performance, as follows :

4.1.1. Stability (Hopf bifurcation) boundary

For feedback gains satisfying $k_1 > 0, k_2 < 0$ the condition $a_1 > 0$ is trivially satisfied, hence the stability boundary is the curve $a_0 = 0$, which is a line on the $k_1 - k_2$ plane, as seen in (48). In the *ideal* case, it is $r = 0$ and V_{ss}, u_{ss} are given by (31), hence we have after some manipulations

$$-N\,\frac{V_{in}}{LC}\cdot k_1 \;-\; 2\frac{V_{ss}}{RLC}\cdot k_2 \;+\; N\,\frac{V_{in}^2}{LCV_{ss}^2} \;>\; 0 \tag{49}$$

4.1.2. Performance specifications

Simple time-domain performance specifications in terms of the linearized model can be also easily set on the basis of typical settling time and overshoot bounds.

A settling time requirement $T_s < T_d$, where T_d a minimum desired time bound, can be expressed as $a_1 > \frac{8}{T_d}$, assuming the well-known formula $T_s = 4/(\zeta\omega_n)$. In the *ideal* case from (48) we have

$$\frac{V_{ss}^2}{RCV_{in}}\cdot k_1 \;-\; \frac{V_{ss}}{L}\cdot k_2 \;+\; \frac{1}{RC} \;-\; \frac{8}{T_d} \;>\; 0 \tag{50}$$

Similarly, a minimum overshoot bound may be set by imposing $\zeta > \zeta_d$, where ζ_d a maximum acceptable damping ratio, and may be expressed as $a_0 < \omega_d^2$, where $\omega_d = \frac{4}{T_d \zeta_d}$. In the *ideal* case from (48) we have

$$-N \frac{V_{in}}{LC} \cdot k_1 \; - \; 2 \frac{V_{ss}}{RLC} \cdot k_2 \; + \; N \frac{V_{in}^2}{LCV_{ss}^2} \; < \; \omega_d^2 \tag{51}$$

It is interesting to observe that the boundary implied by (51) is an expression of the form

$$k_2 \; = \; -N \cdot m \cdot k_1 \; + \; b \tag{52}$$

i.e. a line with negative slope equal to $N \cdot m$ and intercept equal to b, where

$$m = \frac{R \cdot V_{in}}{2\, V_{ss}} \; , \; b = (N \frac{V_{in}^2}{LCV_{ss}^2} - \omega_d^2) \cdot \frac{RLC}{2V_{ss}} \tag{53}$$

suggesting that the number of legs has a direct effect on the minimum overshoot bound, while (50) implies that the settling time requirement is not affected. A similar expression can be also derived for (49), which implies a line boundary with the same slope as in (52) and a different intercept which is proportional to the number of legs N.

4.1.3. Saturation avoidance criteria

Another significant aspect concerning the selection of the controller gains is the saturation avoidance of the control signal. The values of the input voltage, V_{in}, and load resistance, R, are characterised by uncertainty which is summarized in Table 1. The variation of these parameters will give rise to several equilibrium points, as illustrated in Figure 4, which will populate the line segment with the two extreme points p_1 and p_2. Thus, it can be deduced that the feasible equilibria region is given as

$$L = \left\{ \mathbf{x} \,|\, x_1 = V_{ss}, I_{ss}^- \leq x_2 \leq I_{ss}^+ \right\}$$

where I_{ss}^+ and I_{ss}^- can be found by utilizing (17) and the values for the input voltage and load resistance of $p_1 = [V_{ss}\,,\, I_{ss}^+]^T$ and $p_2 = [V_{ss}\,,\, I_{ss}^-]^T$ respectively. In order to ensure saturation avoidance the feasible equilibria region needs to be a subset of the unsaturated region, see [31]. The unsaturated region is delineated by the two saturation lines $u = 0$ and $u = 1$. For the general expression of the control law $u = \mathbf{k}^T(\mathbf{x} - \mathbf{x_{ss}}) +$

u_{ss} these lines can be denoted as $\mathbf{k}^T(\mathbf{x} - \mathbf{x_{ss}}) = -u_{ss}$ and $\mathbf{k}^T(\mathbf{x} - \mathbf{x_{ss}}) = 1 - u_{ss}$. Their distances from the equilibrium point are

$$d_1(\mathbf{k}, u_{ss}) = \frac{u_{ss}}{\sqrt{\mathbf{k}^T\mathbf{k}}},\ d_2(\mathbf{k}, u_{ss}) = \frac{1 - u_{ss}}{\sqrt{\mathbf{k}^T\mathbf{k}}} \tag{54}$$

The distance between the two extreme points p_1 and p_2 can be expressed w.r.t. $\mathbf{k}$ as

$$d_{12}(\mathbf{k}) = \frac{\mathbf{k}^T\,(p_1 - p_2)}{\sqrt{\mathbf{k}^T\mathbf{k}}} \tag{55}$$

The necessary and sufficient condition for saturation avoidance is

$$d_{12}(\mathbf{k}) \leq min\left(d_1(\mathbf{k}, u_{ss}^-)\,,\, d_2(\mathbf{k}, u_{ss}^+)\right) \tag{56}$$

where u_{ss}^- and u_{ss}^+ are the values that correspond to I_{ss}^- and I_{ss}^+ respectively. In this case (56) can be reduce to the simple form

$$|k_2| \leq \frac{min\,(u_{ss}^-\,,\, 1 - u_{ss}^+)}{I_{ss}^+ - I_{ss}^-} \tag{57}$$

The condition described by (57) ensures that the feasible equilibria region is included in the unsaturated region.

4.1.4. A new design method through bifurcation analysis

Following the same approach with [31] we are now in the position to propose a new control law synthesis technique for interleaved boost converters incorporating the previous bifurcation analysis. First, the feasible region in the control gains space is specified such that closed-loop stability (Hopf bifurcation), saturation avoidance, performance specifications and special bifurcation avoidance conditions are met. Second, a control law is selected in an optimal manner, i.e. by maximizing performance related metrics. If the performance of the proposed controller is not satisfactory, this framework allows flexible and transparent re-designs with new specifications to be performed, giving rise to different trade-offs between conflicting goals. This design procedure is explained in more details in the case study presented in section 6. [4]

[4] It is noted that, although all previous results have been obtained for the converter operating under nominal conditions, they can be extended to a wide-range operation case, with extra conditions as in [31].

4.2. *Dynamic state-feedback design using the linearized averaged model*

Our dynamic state-feedback controller is formed with the addition of an extra (integrator) state $x_i = \int_0^t (x_1 - V_{ref})\,\mathrm{d}t$. In this case, the truncated second order system in (39) becomes third order, i.e. we have $\mathbf{x} = [\,x_1\; x_2\; x_i\,]^T$, where $x_1 = V_C$, $x_2 = i_{L1}$ and the new state-space equations and control law are given by (58) and (59), respectively. The expression of the control law in this case is relieved of the set-point terms due to the action of the integrator.

$$\dot{\mathbf{x}} = \begin{cases} -\frac{x_1}{R\,C} + \frac{N\,x_2}{C} - u\,\frac{N\,x_2}{C} \\ -\frac{x_1}{L} - \frac{r\,x_2}{L} + u\,\frac{x_1}{L} + \frac{V_{in}}{L} \\ x_1 - V_{ref} \end{cases} \tag{58}$$

$$u_1 = k_1\,x_1 + k_2\,x_2 + k_i\,x_i \tag{59}$$

The same steady-state values as in (13),(17) are then obtained for $V_{ss} = V_{ref}$ in the domain of interest $[0\;, u_{ss}^{max}]$, i.e.

$$u_{ss} = 1 - \frac{V_{in} + \sqrt{\frac{N\,R\,V_{in}^2 - 4\,r\,V_{ref}^2}{N\,R}}}{2\,V_{ref}} \tag{60}$$

$$I_{ss} = \frac{V_{in} - \sqrt{V_{in}^2 - \frac{4\,r\,V_{ref}^2}{N\,R}}}{2\,r} \tag{61}$$

Substituting (59) in (58) and linearizing around the equilibrium point for the error dynamics $\mathbf{x}_e$ and input u_e we arrive at

$$\mathbf{A}_{lin} = \begin{bmatrix} -\frac{1}{RC} - \frac{NI_{ss}k_1}{C} & \frac{N(1-d_{ss}-I_{ss}k_2)}{C} & -\frac{NI_{ss}k_i}{C} \\ -\frac{1-d_{ss}-V_{ss}k_1}{L} & -\frac{r-V_{ss}k_2}{L} & \frac{V_{ss}k_i}{L} \\ 1 & 0 & 0 \end{bmatrix} \tag{62}$$

$$\dot{\mathbf{x}}_e = \begin{bmatrix} -\frac{1}{RC} & \frac{N}{C}(1-d_{ss}) & 0 \\ -\frac{1}{L}(1-d_{ss}) & -\frac{r}{L} & 0 \\ 1 & 0 & 0 \end{bmatrix} \mathbf{x}_e + \begin{bmatrix} \frac{NI_{ss}}{C} \\ -\frac{V_{ss}}{L} \\ 0 \end{bmatrix} u_e \tag{63}$$

The same holds for the constrained stabilization setting and the stability validation procedure using flexible piecewise-linear Lyapunov functions adopted in that paper. These techniques are omitted in this work due to space limitations.

5. Digital control law implementation

In general, for an N-leg converter, the leg currents are sampled with a sampling frequency f_s equal to the switching frequency, with the appropriate phase shift, whereas for the output voltage a higher sampling frequency of $N \cdot f_s$ has to be used. The *analog* state feedback control laws designed in the previous section for a 2-leg topology are *digitally* implemented as shown in Figure 5 (top) and implied by both (64) and (65). Both currents are sampled every $T = 1/f_s$ seconds (with a phase shift of $T/2$ for the second current), while the voltage is sampled every $T/2$ seconds.

$$u_1[nT] = k_1(x_1[nT] - x_{1,ref}) + k_2(x_2[nT] - x_{2,ref}) + d_{ss} \tag{64}$$

$$\begin{aligned} u_2\left[nT + \frac{T}{2}\right] \;=\; & k_1\left(x_1\left[nT + \frac{T}{2}\right] - x_{1,ref}\right) \\ & + k_2\left(x_3\left[nT + \frac{T}{2}\right] - x_{3,ref}\right) + d_{ss} \end{aligned} \tag{65}$$

Accordingly, the digital implementation of a *dynamic* state-feedback control law is depicted in Figure 5 (bottom) and the related control expressions are given in (66) and (67).

$$u_1\left[nT\right] \;=\; k_1\, x_1\left[nT\right] \;+\; k_2\, x_2\left[nT\right] \;+\; k_i x_i\left[nT\right] \tag{66}$$

$$\begin{aligned} u_2\left[nT + \frac{T}{2}\right] \;=\; & k_1\, x_1\left[nT + \frac{T}{2}\right] + k_2\, x_3\left[nT + \frac{T}{2}\right] \\ & + k_i\, x_i\left[nT + \frac{T}{2}\right] \end{aligned} \tag{67}$$

These expressions can be directly utilized to simulate the operation of the system. In fact, the simulation results presented in the next section were obtained by making use of the corresponding diagrams shown in Fig. 5 in $SIMULINK^{TM}$. However, when it comes to the real implementation of control laws the control signals are delayed until the next sampling time instant.

For sampling frequencies $f_s = 10$ KHz or higher both numerical and experimental results confirm that the digital implementation of the continuous-time design is reliable. The sampling frequency is considerably high compared to the converter's dynamics,

Parameter	Value	Nominal value
R	$[20\,,\,80]\,\Omega$	$40\ \Omega$
V_{in}	$[3.5\,,\,6.5]\,\mathrm{V}$	$5\,\mathrm{V}$
u_{ss}	0.5264	0.5264
L	1 mH	1 mH
C	$20\,\mu F$	$20\,\mu F$
r	$1\,\Omega$	$1\,\Omega$
N	2	2

Table 1: Interleaved Boost Converter Parameters.

and as such the effects of the digital implementation are negligible, hence the digitally controlled system behaves closely to its continuous counterpart.

6. An illustrative design example

We consider an interleaved boost converter with $N = 2$ legs as in Figure 1 with nominal parameter values $L = 1$ mH, $r = 1\,\Omega$, $C = 20\,\mu$F, $R = 40\,\Omega$, $V_{in} = 5\,$V, $V_{ref} = 10\,$V. We also consider large parameter variations as shown in Table 1. A number of control laws have been designed for this system to test the ideas described in the previous sections. The proposed designs have been verified using the exact switched model of the converter with numerical simulation in $SIMULINK^{TM}$. Furthermore, they have been also experimentally tested using a prototype interleaved converter and a hardware digital implementation using Labview on board a NI SBRIO 9636 FPGA device from National Instruments. The inductor current sensor used in each leg was chosen to be a LEM LTS 6-NP.

6.1. Open-loop experiments

The first experiment conducted had the purpose of identifying the inductor series resistance. As seen from the steady-state voltage and current expressions in (13), the series resistance has a significant impact which cannot be overlooked. For this reason, acquiring a good estimate of the internal resistance value, through an experimental

procedure, is a necessity. The result of this experimental identification procedure is depicted in Figure 6, where equation (13) was used for applying a proper curve fitting technique, taking r as the variable to be chosen for the curve to best fit the real data. It should be noted that r does not represent the inductor series resistance only, although it is modeled that way, but it also represents other losses that may stem from other components of the system. The resulting value of the resistance was found to be $r = 0.9936\Omega$, rounded up to 1Ω for simplicity.

6.2. Pole placement using the linearized averaged dynamics

We begin our control law evaluation procedure with the simplest control design, i.e. a simple pole placement using a 2nd order linearized model, according to the process outlined in subsection 4.1. The design is based on the selection of the desired damping factor ζ, natural frequency ω_n and corresponding settling time T_s values, for the polynomial in (48). Then the analysis of section 3 can be applied in order to check for the existence of multiple equilibria in the operating region of interest.

The performance specifications are adopted from [32], which provide a fast oscillation-free transient response. A damping factor $\zeta = 0.707$ and a natural frequency $\omega_n = 2.830$ rad/sec (corresponding to a settling time $T_s = 2$ msec, assuming that $T_s \simeq 4/\zeta\omega_n$) are chosen which will provide the desired transient response. With $V_{ss} = 10$ V the corresponding values of u_{ss}, I_{ss} are found from (13),(16) to be $u_{ss} = 0.5264$, $I_{ss} = 0.2639$ A and the poles are placed at $s_{1,2} = -\zeta\,\omega_n \pm \omega_n\sqrt{1-\zeta^2} = -2000 \pm j2000$. The corresponding gains of this pole placement procedure are found to be $\mathbf{k} = [0.0391 \quad -0.0719]^T$.

6.3. Bifurcation analysis for static state-feedback laws

The gains specified by the previous pole placement procedure may give rise to multiple equilibria. This can be easily checked using the analysis in section 3. Further stability and performance criteria can be addressed using the conditions described in section 4.

For the parameter variations given in Table 1 the feasible region on the gain space k_1–k_2 is shown below in Figure 7.

The corresponding bifurcation curve is plotted as a dashed line. This curve is not an approximation since it is calculated using the bilinear model. Further curves shown are the $\zeta = 0.5$, $T_s = 2$ msec, saturation avoidance of the control signal, and the (Hopf bifurcation) stability boundary, which are approximate since they are determined numerically using the linearized model. Figure 7 can facilitate the selection of appropriate gains, that satisfy desired performance requirements as well as avoidance of multiple equilibria.

The bifurcation curve in Fig. 7 suggests that the gains $k_1 = 0.0391$, $k_2 = -0.0719$ (marked with a "*") which have been selected before lay outside the safe region of a single equilibrium (designated as "EQ1" in Figure 7). In fact, one can calculate that there exist three equilibria at $10,\ 17.1707,\ 22.023$ Volts. The two equilibria at 10 and 22.03 Volts correspond to stable nodes, whereas the third one at 17.17 Volts is a saddle point.To illustrate the problematic situation that can arise when the gains lay in the multiple equilibria region, a representative simulation experiment shown in Figure 8 has been carried out.

In Fig. 8 a startup transient is initially shown, in which the system operates inside the region of attraction of the first node. However, in the case of a large load disturbance for a short time period the system trajectory eventually exceeds the saddle point and lays in a region where it is diverted to the second stable node, at significantly higher output voltage and leg current values. This is a potentially hazardous situation that can be avoided by using the bifurcation analysis of subsection 3.

It is worth noting that this undesirable situation may occur much more easily for an even more unfortunate selection of the feedback gains. If new gains farther outside the single equilibria EQ1 region are selected, e.g. $k_1 = 0.06$, $k_2 = -0.2$ (marked with a "+" in Figure 7), the multiple equilibria are moved to $10,\ 10.5,\ 22.5$ Volts, i.e. the saddle point is located at 10.5 Volts, really close to the neighbourhood of the stable desired equilibrium at 10 Volts! This implies that a sudden slight disturbance could severely affect the system's operation. To illustrate this phenomenon representative simulation and experimental results are shown in Figure 9. The system is initially at normal operating conditions, however when the system is subjected to a sudden slight load disturbance for a short time period the system trajectory is immediately attracted

by the saddle point to a distant operating point corresponding to the second stable node.

Along these lines we modified the initial design, and picked new values $k_1 = 0.03$, $k_2 = -0.2$ (marked with an "x"), which are far from the bifurcation curve, and also correspond to a reasonable damping factor value $0.5 \leq \zeta \leq 1$, a sufficiently high natural frequency $\omega_n > 3000$ rad/sec and abide by the saturation avoidance condition. In fact, the new selection places the closed-loop poles at $-2521 \pm j\,2985$ with $\zeta = 0.645$ and $\omega_n = 3907$ rad/sec.

For a switching frequency $f_s = 20$ KHz, and under *static* state-feedback control, the evolution of the output voltage of the converter at start-up is shown in Figure 10. Simulated responses from the exact switched model and the bilinear averaged model are also plotted. The two simulated responses are quite close to each other, and would certainly come closer for an increased switching frequency. The experimental response is very satisfactory.

6.4. Dynamic state-feedback pole placement

In the dynamic state feedback case we do not expect any multiple equilibria, due to the presence of an integrator. In the case where the state feedback gains are chosen to place the poles of the system in the left half of the complex plane the operation of the integrator will always try to diminish any error between the desired voltage reference, V_{ref}, and the voltage of the converter. However, what needs to be taken into account is the value of the reference signal which should never exceed V_{ss}^{max}. If the reference signal were to exceed that value an integrator wind-up situation would be instigated. Along these lines it can be deduce that for $V_{ref} \in [0\,,\, V_{ss}^{max}]$ there will always be a single equilibrium and the control design procedure is no longer confined by constraints concerning multiple equilibria. A pole placement procedure based on the linearized state-space equations (63) can be applied in order to calculate the three gains $k_1,\, k_2,\, k_i$. The desired location of the closed-loop poles is adopted from [32], which lay at $-2000 \pm j\,1000\,,\, -5000$, so that a pair of dominant complex poles with $\zeta = 0.89$ and $\omega_n = 2236$ rad/sec is obtained. The resulting gain values that drive the poles of the system to the desired location are $k_1 = 0.0274,\, k_2 = -0.6026,\, k_i = -56$.

The performance of this *dynamic* state-feedback control law is depicted in Figs. 11, 12. The disturbance rejection behavior of the controller is tested against large load and set-point step changes. The results are quite satisfactory and the close resemblance of the simulated with the experimental responses suggests a successful proof of concept for the simple pole-placement control design procedures used in this work.

7. Discussion and conclusions

This work has dealt with the design of both static and dynamic full state-feedback controllers for compensating a multi-phase interleaved converter. Pole placement techniques have been proposed which are based on the linearized averaged dynamics of the bilinear interleaved converter. Their performance has been verified by simulation and experimental results. We have shown that the averaged model plays an important role on the controller's gain selection procedure and can provide a reasonably good approximation on potential multiple equilibrium points, in the case of static state-feedback. It is also reported that, although very useful in other respects, the interleaving process leads to more serious bifurcation phenomena, such as multiple equilibria, as the number of phases is increased. To deal with this problem, a complete bifurcation analysis procedure has been developed to serve as a complementary tool in the design process so that multiple equilibria can be completely avoided or ruled out of the operating region of interest.

References

[1] M. di Bernardo, C. Budd, A. R. Champneys, P. Kowalczyk, Piecewise-smooth Dynamical Systems, Springer-Verlag, London, 2008.

[2] C. K. Tse, Complex Behavior of Switching Power Converters, CRC Press, Boca Raton, USA, 2003.

[3] S. Banerjee, G. C. Verghese (Eds.), Nonlinear Phenomena in Power Electronics: Attractors, Bifurcations, Chaos, and Nonlinear Control, IEEE Press, New York, 2001.

[4] E. Aroudi, D. Giaouris, H. H. C. Iu, I. A. Hiskens, A review on stability analysis methods for switching mode power converters, IEEE Journal on Emerging and Selected Topics in Circuits and Systems 5 (2015) 302–315. doi:doi: 10.1109/JETCAS.2015.2462013.

[5] A. Beccuti, S. Mariethoz, S. Cliquennois, S. Wang, M. Morari, Explicit model predictive control of DC-DC switched-mode power supplies with extended Kalman filtering, Industrial Electronics, IEEE Transactions on 56 (6) (2009) 1864–1874.

[6] S. Mariethoz, et al, Comparison of hybrid control techniques for buck and boost DC-DC converters, IEEE Transactions on Control Systems Technology 18 (5) (2010) 1126–1145.

[7] P. Karamanakos, T. Geyer, S. Manias, Direct model predictive current control strategy of DC-DC boost converters, IEEE Journal of Emerging and Selected Topics in Power Electronics 1 (4) (2013) 337–346.

[8] V. Spinu, N. Athanasopoulos, M. Lazar, G. Bitsoris, Stabilization of bilinear power converters by affine state feedback under input and state constraints, IEEE Transactions on Circuits and Systems-II Express Briefs 59 (8) (2012) 520–524.

[9] C. Olalla, I. Queinnec, R. Leyva, A. E. Aroudi, Robust optimal control of bilinear DC-DC converters, Control Engineering Practice 19 (2011) 688–699. doi:10.1016/j.conengprac.2011.03.004.

[10] C. Olalla, R. Leyva, I. Queinnec, D. Maksimovic, Robust Gain-Scheduled Control of Switched-mode DC-DC Converters, IEEE Transactions on Power Electronics 27 (2012) 3006–3019. doi:10.1109/TPEL.2011.2178271.

[11] C. Olalla, I. Queinnec, R. Leyva, A. E. Aroudi, Optimal state-feedback control of bilinear DC-DC Converters with guaranteed regions of stability, IEEE Transactions on Industrial Electronics 59 (2012) 3868–3880. doi:10.1109/TIE.2011.2162713.

[12] T. Hu, A nonlinear-system approach to analysis and design of power-electronic converters with saturation and bilinear terms, IEEE Transactions on Power Electronics 26 (2011) 399–410. doi:10.1109/TPEL.2010.2054115.

[13] C. Olalla, R. Leyva, A. E. Aroudi, I. Queinnec, Robust LQR control for PWM converters: An LMI approach, IEEE Transactions on Industrial Electronics 56 (2009) 2548 – 2558. doi:10.1109/TIE.2009.2017556.

[14] R. Leyva, C. Ollala, I. Queinnec, S. Tarbouriech, C. Alonso, L. M. Salamero, Passivity-based control for large-signal stability of high-order switching converters, Asian Journal of Control 4 (2) (2012) 335–347.

[15] A. Cid-Pastor, L. Martinez-Salamero, A. E. Aroudi, J. Giral, R. Calvente, R. Leyva, Synthesis of loss-free resistors based on sliding-mode control and its applications in power processing, Control Engineering Practice 21 (2013) 689–699.

[16] B. Banerjee, R. M. Kotecha, W. W. Wayne W. Weaver, Digital memory look-up based implementation of sliding mode control for DC-DC converters, Control Engineering Practice 54 (2016) 1–11.

[17] A. Belkaid, J.-P. Gaubert, A. Gherbi, L. Rahmani, Maximum power point tracking for photovoltaic systems with boost converter sliding mode control, in: IEEE International Symposium on Industrial Electronics (ISIE), 2014, pp. 556–561.

[18] U. Sadek, A. Sarjas, A. Chowdhury, A. Svecko, FPGA-based optimal robust minimal-order controller structure of a DC - DC converter with pareto front solution, Control Engineering Practice 55 (2016) 32–44.

[19] F. Ounis, N. Golea, Mu - synthesis based robust voltage control for cascade boost power converter, in: IEEE International Conference on Control, Engineering and Information Technology (CEIT), 2015, pp. 1–6.

[20] M. Truntic, M. Milanovic, K. Jezernik, Model predictive control of a DC-DC converter for battery emulation, Control Engineering Practice 19 (5) (2011) 502–512.

[21] P. Karamanakos, T. Geyer, S. Manias, Model predictive control of the interleaved DC-DC boost converter with coupled inductors, in: European Conference on Power Electronics and Applications (EPE), 2013, pp. 1–10.

[22] R. Cisneros, M. Pirro, G. Bergna, R. Ortega, G. Ippoliti, M. Molinas, Global tracking passivity-based PI control of bilinear systems: Application to the interleaved boost and modular multilevel converters, Control Engineering Practice 43 (2015) 109–119.

[23] H. A. Bouziane, R. B. Bouiadjra, M. B. Debbat, Design of robust LQR control for DC-DC multilevel boost converter, in: IEEE International Conference on Electrical Engineering (ICEE), 2015, pp. 1–5.

[24] N. Bouhalli, M. Cousineau, E. Sarraute, T. Meynard, Multiphase coupled converter models dedicated to transient response and output voltage regulation studies, in: 13th International Power Electronics and Motion Control Conference (EPE-PEMC), 2008, pp. 281 – 287.

[25] D. Neacsu, W. Bonnice, E. Holmansky, On the small-signal modeling of parallel/interleaved buck/boost converters, in: IEEE Int. Symposium on Industrial Electronics, ISIE, 2010, pp. 2708 – 2713.

[26] H. Fadil, F. Giri, J. M. Guerrero, B. Salhi, Adaptive control of interleaved boost converter for fuel cell energy, in: ACC, 2011, pp. 3905 – 3910.

[27] A. Schittler, D. Pappis, R. C., C. A., M. Dalla Costa, Generalized state-space model for the interleaved buck converter, in: Brazilian Power Electronics Conference (COBEP), 2011, pp. 451 – 457.

[28] P. Strumpf, A. Lorincz, I. Nagy, Stability of digitally controlled pfc boost converter with auxiliary state vector, in: IEEE International Symposium on Industrial Electronics (ISIE), 2013, pp. 1–6.

[29] C. Yfoulis, D. Giaouris, S. Voutetakis, S. Papadopoulou, Constrained switching stabilization of a DC-DC boost converter using piecewise-linear Lyapunov functions, in: IEEE MED, 2013, pp. 814–823.

[30] C. Yfoulis, D. Giaouris, F. Stergiopoulos, C. Ziogou, S. Voutetakis, S. Papadopoulou, Robust constrained stabilization of a boost DC-DC converter with Lyapunov-based control and piecewise-linear Lyapunov functions, in: European Control Conference (ECC), 2014, pp. 2170–2175.

[31] C. Yfoulis, D. Giaouris, F. Stergiopoulos, C. Ziogou, S. Voutetakis, S. Papadopoulou, Robust constrained stabilization and tracking of a boost DC-DC converter through bifurcation analysis, Control Engineering Practice 35 (February 2015) 67–82.

[32] G. Gkizas, C. Amanatidis, D. Giaouris, C. Yfoulis, F. Stergiopoulos, C. Ziogou, S. Voutetakis, S. Papadopoulou, State-feedback control of an interleaved DC-DC boost converter, in: IEEE Mediterranean Conference on Control and Automation (MED), 2016, pp. 931 – 936.

[33] R. Leyva, L. Martinez-Salamero, H. Valderrama-Blavi, J. Maixe, R. Giral, F. Guinjoan, Linear state-feedback control of a boost converter for large-signal stability, IEEE Transactions on Circuits and Systems I: Fundamental Theory and Applications 48 (4) (2001) 418–424. doi:10.1109/81.917979.

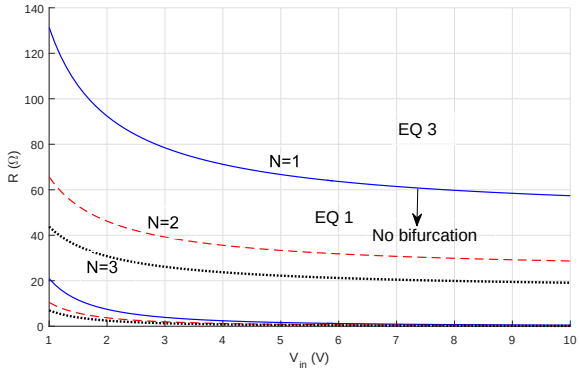

(a)

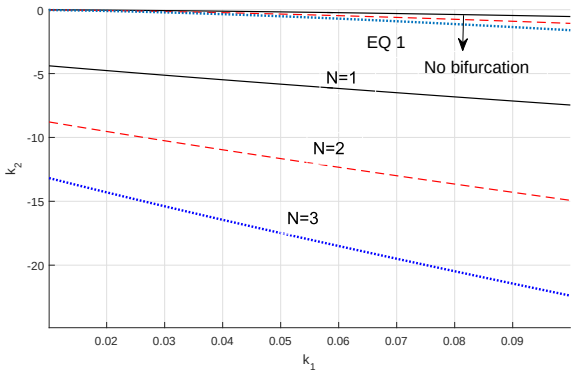

(b)

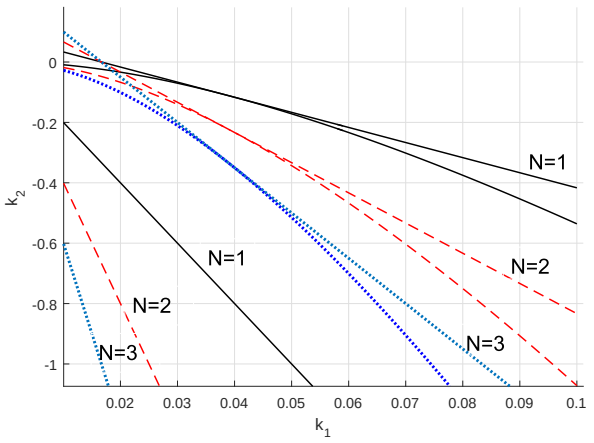

(c)

Figure 2: Representative bifurcation diagrams for the converter of section 6 in the ideal case with $V_{in} = 5$ V, $V_{ss} = 10$ V, $V_C^+ = 30$ V, $R = 40\,\Omega$, $r = 0$ and $N = 1$ (solid), $N = 2$ (dashed),$N = 3$ (dotted). (a) $V_{in} - R$ diagram for gain $\mathbf{k}_2 = [0.0443, -0.2324]^T$, (b) $k_1 - k_2$ diagram (global view with bifurcation curves $\Gamma = 0$ only) , and (c) detailed $k_1 - k_2$ diagram with bifurcation curves and lines. In (a) and (b) the absence of bifurcations is valid in the area enclosed by the bifurcation curves corresponding to the different cases where N=1,2,3. In (c) the magnification of the area of interest along with the curves provided by Lemmas 1 and 2 are portrayed.

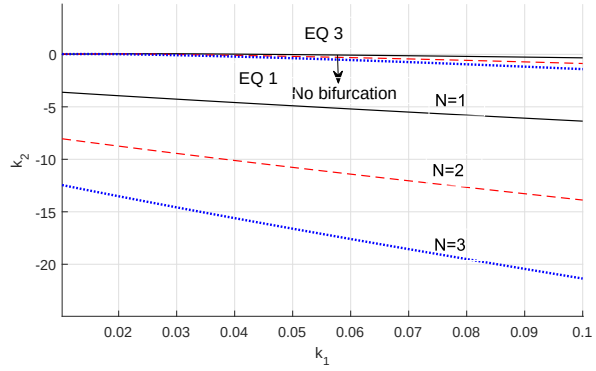

(a)

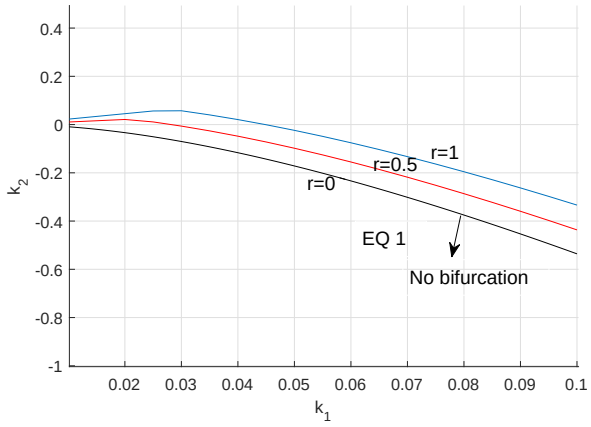

(b)

Figure 3: Representative $k_1 - k_2$ bifurcation diagrams for the converter of section 6 with $V_{in} = 5$ V, $V_{ss} = 10$ V, $R = 40\,\Omega$ in the non-ideal case. (a) Bifurcation curves $\Gamma = 0$ for $r = 1$ and $N = 1$ (solid), $N = 2$ (dashed), $N = 3$ (dotted), and (b) Bifurcation curves $\Gamma = 0$ for $N = 1$ and variable $r = 0, 0.5, 1\,\Omega$.

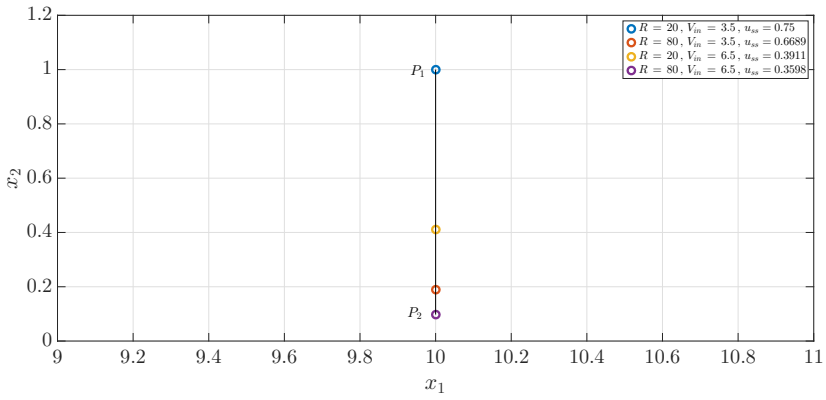

Figure 4: The feasible equilibria region and the two extreme points p_1, p_2.

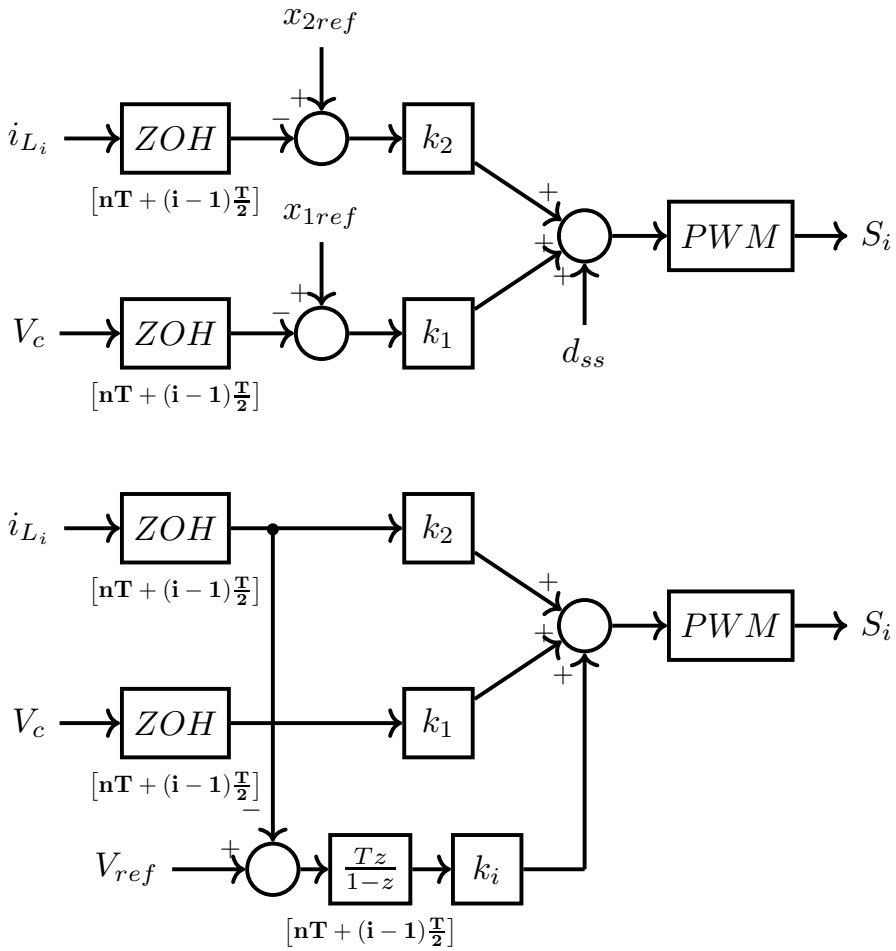

Figure 5: Digital implementation of a static and a dynamic state-feedback control law for a two legged interleaved DC-DC boost converter, for $i = 1, 2$.

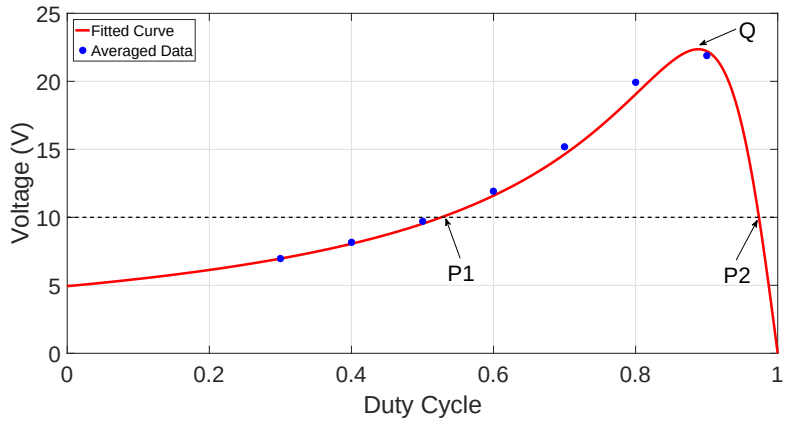

Figure 6: Series resistance estimation procedure based on curve fitting.

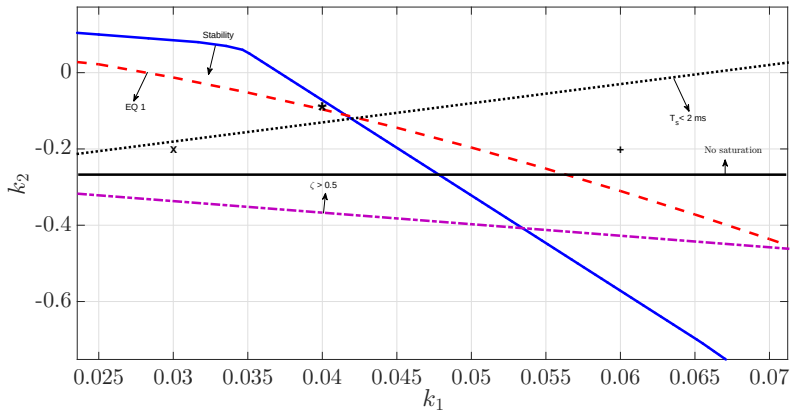

Figure 7: Feasibility conditions on the k_1–k_2 plane. The curves are boundaries for (a) Hopf bifurcation (solid), (b) Multiple equilibria bifurcation (dashed), (c) Settling time $T_s = 2$ msec (dotted), (d) Damping factor $\zeta = 0.5$ (dash-dotted), (e) saturation avoidance (solid). The arrows point out to the feasible subspace, where the corresponding criteria or specs are met for all parameter values of Table 1.

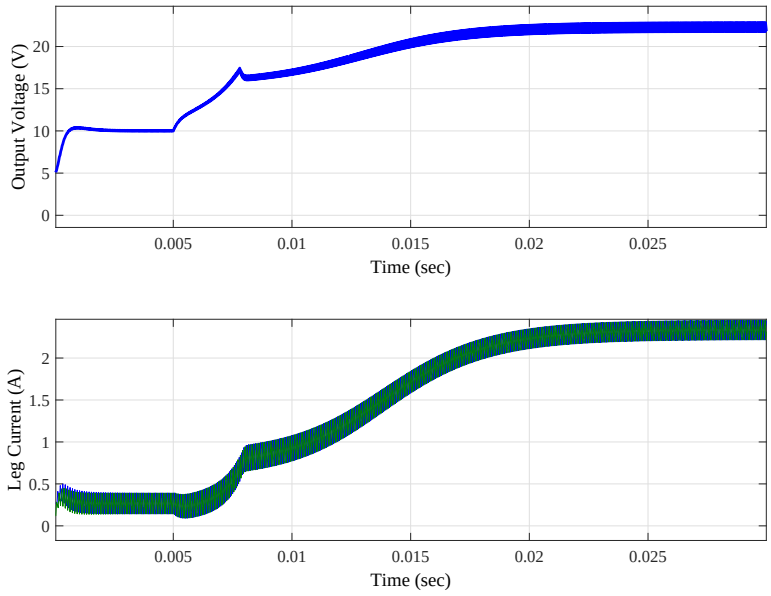

Figure 8: Output voltage and leg inductor currents for an initial startup transient to 10 Volts and a subsequent load transient from $R = 40\,\Omega$ to 80 Ω for 3 msec (from $t_1 = 0.005$ to $t_2 = 0.008$ sec), and then back to $R = 40\,\Omega$, for $f_s = 20$ KHz. The gains used are $k_1 = 0.0391$, $k_2 = -0.0719$.

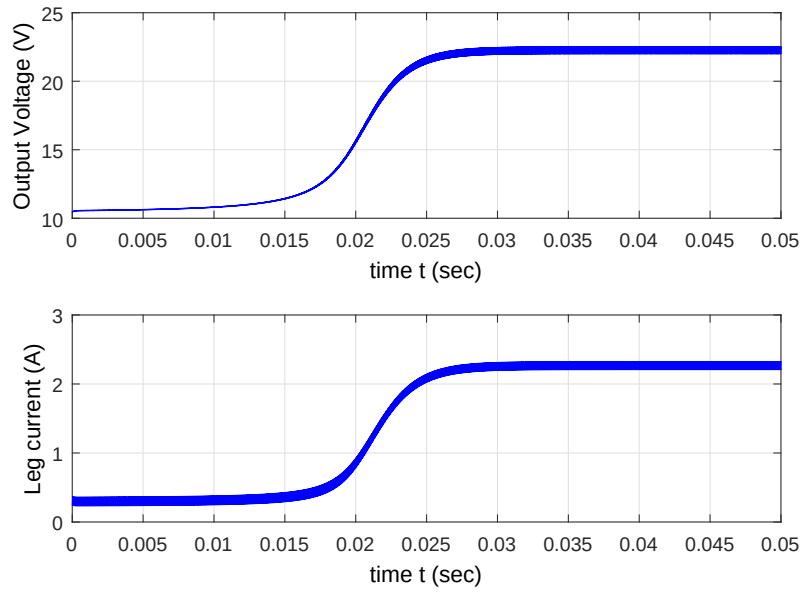

(a)

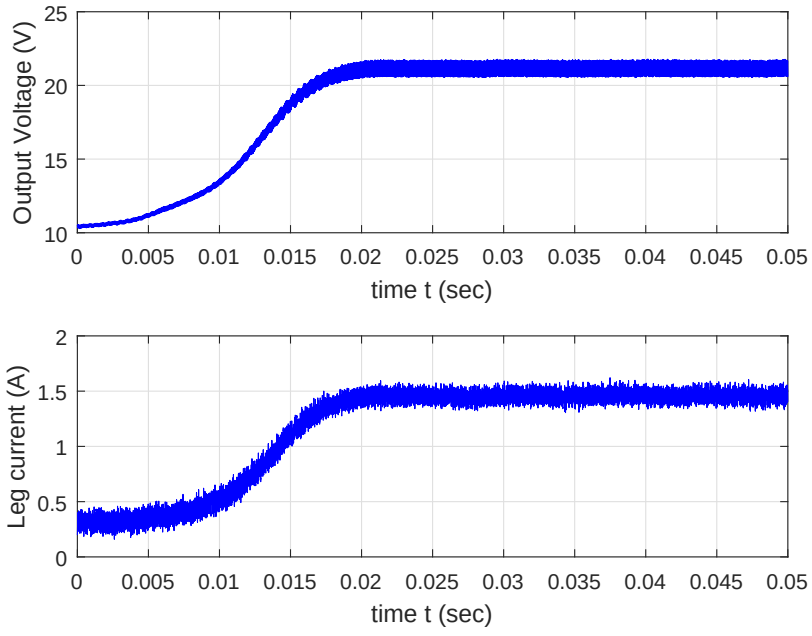

(b)

Figure 9: Output voltage and leg inductor current for a sudden load transient (from normal operation at 10 Volts) and another set of gains $k_1 = 0.06$, $k_2 = -0.2$, for $f_s = 20$ KHz. (a) Simulation results, (b) Experimental results.

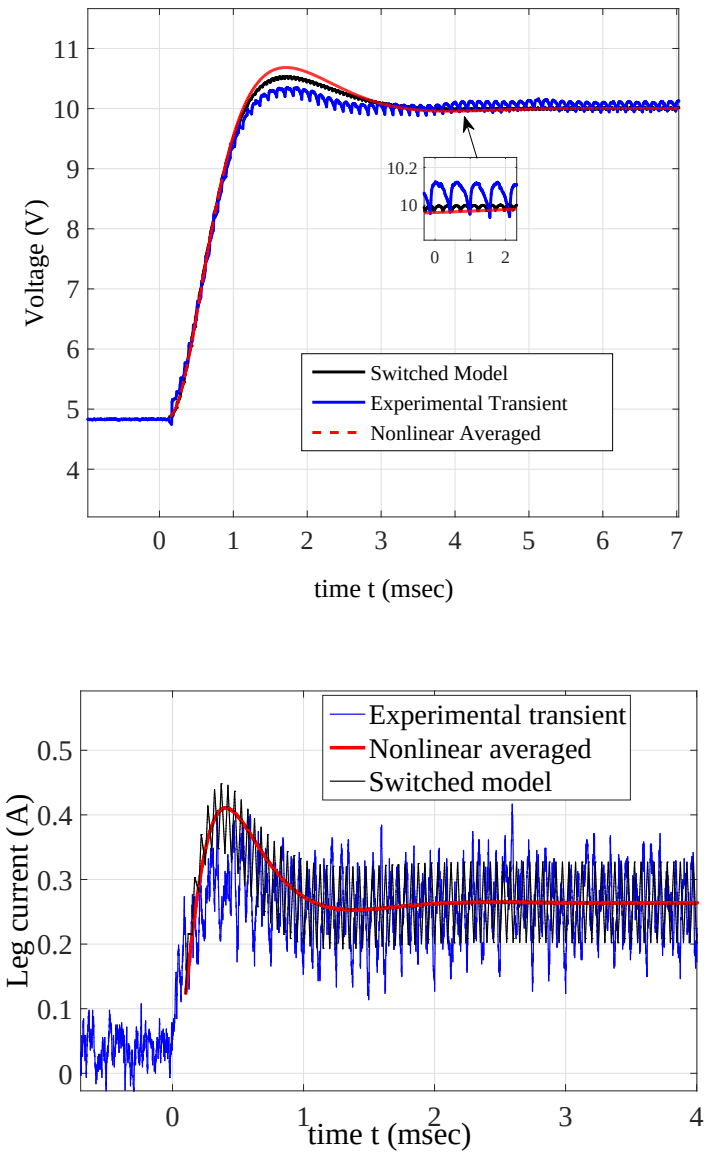

Figure 10: Startup transient response of our interleaved DC-DC boost converter under static state feedback with $\mathbf{k} = [-0.03\ 0.2]^T$ and $f_s = 20$ KHz. Simulation vs experimental results.

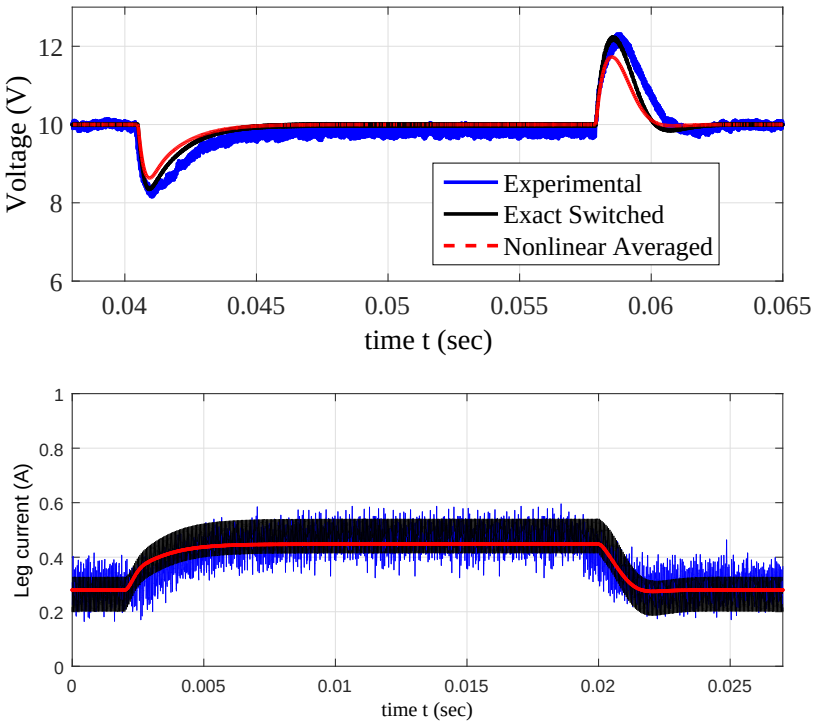

Figure 11: Load transient response of our interleaved DC-DC boost converter under dynamic state-feedback with $f_s = 10$ KHz and $\mathbf{k} = [0.0274 \ -0.6026 \ -56]^T$ (top) , $f_s = 20$ KHz (bottom). Simulation vs experimental results. The load is changed twice, from $R = 40\Omega$ to $R = 20\Omega$ and then back again to 40Ω.

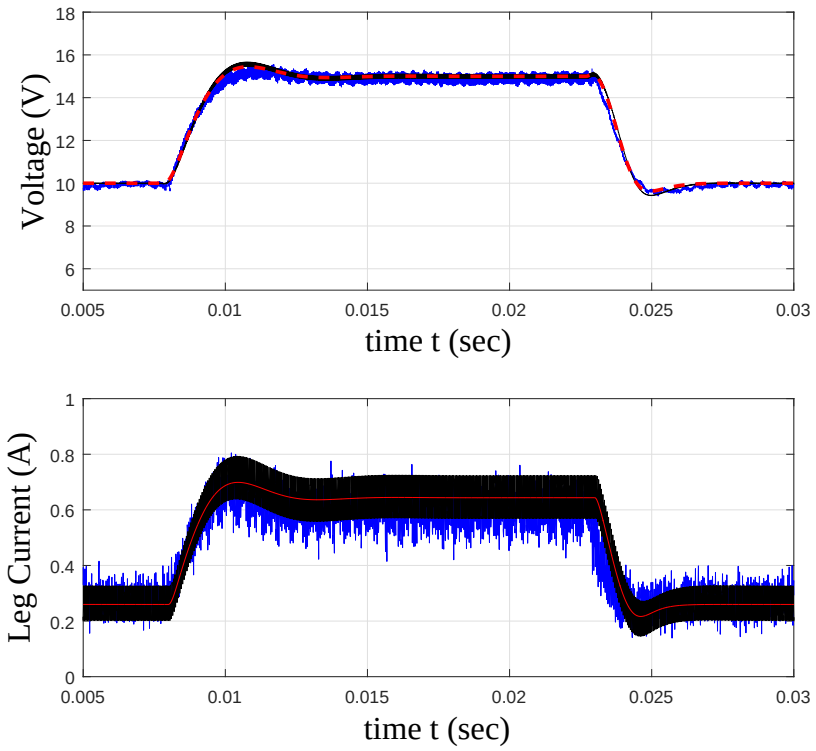

Figure 12: Set-point change transient response of our interleaved DC-DC boost converter under dynamic state-feedback for $f_s = 20$ KHz and a set of gains $\mathbf{k} = [0.0274 \ -0.6026 \ -56]^T$. Simulation vs experimental results.